Onset of small-scale instabilities at the base of the lithosphere : scaling laws and role of pre-existing structures

Caroline Dumoulin, Doin M.P., D. Arcay, L. Fleitout

Geophys. J. Int. (2005) **160,** 344–356 doi: 10.1111/j.1365-246X.2004.02475.x

Onset of small-scale instabilities at the base of the lithosphere: scaling laws and role of pre-existing lithospheric structures

Caroline Dumoulin,[1] Marie-Pierre Doin,[2] Diane Arcay[2] and Luce Fleitout[2]

[1] *Laboratoire de Planétologie et Géodynamique, Université de Nantes,* 2 *rue de la Houssinière,* PO Box 92208,44322 *Nantes Cedex* 3, *France. E-mail: Caroline.Dumoulin@chimie.univ-nantes.fr*

[2] *Laboratoire de Géologie, Ecole Normale Supérieure,* 24 *rue Lhomond,* 75231 *Paris Cedex* 05, *France*

Accepted 2004 September 17. Received 2004 July 28; in original form 2004 April 14

SUMMARY

Numerical simulations of 2-D Rayleigh–Bénard convection are designed to study the development of convection at the base of the cooling lithosphere. A zero temperature is suddenly imposed at the mantle surface, which has initially a homogeneous temperature. The strongly temperature-dependent viscosity fluid is heated from within, in order to balance the internal temperature drift resulting from global fluid cooling. For a while, the lithosphere cools approximatively as a conductive half-space and the lithospheric isotherms depth grows as the square root of age. As instabilities progressively develop at the base of the lithosphere, lithospheric cooling departs from the half-space model. We propose two different parametrizations of the age of the first dripping instability, using boundary layer marginal stability or quantifying the characteristic timescale of the instability exponential growth as a function of the Rayleigh number and of the viscous temperature scale. Both parametrizations account very well for our numerical estimates of onset times, but with a slightly better adjustment of the viscous temperature scale dependence in the second case. The absolute value of the onset time depends on the amplitude and location of initial temperature perturbations within the box and on the initial temperature structure of the thermal boundary layer (TBL). Furthermore, thermal perturbations of finite amplitude located within the lithosphere (such as the ones induced by transform faults, for example) strongly reduce the age of the first dripping instability. However, the onset time parametrization derived from transient cooling experiments well adjusts the lithospheric age of the first drip instability below a lithosphere cooling perpendicularly to the ridge axis. This study emphasizes the role of the initial topography of the lithospheric isotherms on the development of instabilities.

Key words: convection, oceanic lithosphere, transform faults, viscosity.

1 INTRODUCTION

Large-scale convection features on Earth are associated with hot spots, ridges and subduction zones. The oceanic lithospheric cooling is a primary consequence of large-scale convection currents. However, smaller scale convection currents may be superimposed on the large-scale flow. This secondary flow should develop because the base of the lithosphere, the Earth upper thermal boundary layer (TBL),becomes unstable.

Secondary convection is observed in numerical and analogical experiments, under a very wide range of conditions, whatever the geometry or the heating mode. The quasi-static equilibrium state without large-scale convection has long been studied. It consists of a highly time-dependent flow originating from drips that develop at the base of the cold boundary layer. Because cold Earth material is rigid, these developing instabilities only affect the base of the lithosphere (Morris & Canright 1984). Their associated heat transfer scaling laws are now well constrained over a wide parameter range (Davaille & Jaupart 1993; Solomatov 1995; Dumoulin *et al.* 1999; Reese *et al.* 1999; Solomatov & Moresi 2000). However, there is still a debate regarding the conditions under which drips would develop at the base of the Earth lithosphere. From a physical point of view, it is clear that a lithosphere with a growing thickness should, at one point, undergo small-scale convection at its base. It is not clear however, whether the lithosphere could reach this point by cooling before being subducted (for the oceanic lithosphere) or by cooling and/or tectonic thickening (for the continental lithosphere). Therefore, it is critical to constrain the lithospheric age from which drips begin to develop at the base of a growing lithosphere. The physical mechanisms that control this first drip development are not yet well understood. There is still also considerable debate concerning the scaling law describing the minimum lithospheric age for which secondary convection should

develop (Richter & Parsons 1975; Fleitout & Yuen 1984; Buck 1985; Davaille & Jaupart 1994; Choblet & Sotin 2000; Huang *et al.* 2003; Korenaga & Jordan 2003).

On the other hand, some geophysical studies based on seismic anisotropy (Montagner 2002) or on observations of gravity lineations (Haxby & Weissel 1986) suggest that small-scale convection occurs under oceanic lithospheres. Furthermore, the half-space cooling model of the oceanic lithosphere is unable to reproduce the observed heat flow and subsidence variations with age (Parsons & Sclater 1977; Stein & Stein 1992; Doin & Fleitout 1996). The heat flow, subsidence and geoid flattening with age implies that a heat flow is brought from the mantle to the lithosphere during its cooling through small-scale convection, rather than being of deep mantle dynamic origin (Colin & Fleitout 1990; Doin & Fleitout 1996).

Several transient cooling studies have been performed to quantify the onset of small-scale convection. They consist of analysing the evolution of a hot fluid cooled from above that would represent the mantle cooling in sections parallel to the ridge. This problem has been tackled, theoretically as well as numerically and experimentally, for 2-D or 3-D geometries and with different rheologies (Davaille & Jaupart 1994; Choblet & Sotin 2000; Dumoulin 2000; Huang *et al.* 2003; Korenaga & Jordan 2003). However, some disagreements persist, particularly on the onset time parametrization as a function of mantle properties. The mechanism controlling the first drip development and its scaling law has often been assumed to be the marginal stability state of the lithosphere at small-scale convection onset. However, we will show here, following the original idea of Yuen & Fleitout (1984), that the growth rate of the drip at least partially controls the first drip development. Understanding the destabilization mechanism is important when simple transient cooling simulations are applied to the complex geometries of the oceanic lithosphere. Indeed, the oceanic lithosphere isotherms present a permanent topography, at least induced by cooling and transform faults. This topography is a departure from the usually studied flat topography case and reduces the age for the onset of small-scale instabilities (Dumoulin 2000; Huang *et al.* 2003).

In a first section, we will describe the setup of our numerical simulations. In the second part of this paper, we introduce new scaling laws for the onset time of convection in a hot fluid cooled from above. Two different laws are developed: one follows the usual approach of the boundary layer stability analysis (Howard 1964; Davaille & Jaupart 1994; Choblet & Sotin 2000), but we adapted the theoretical parametrization to large viscosity contrasts; the other is based on the perturbation growth rates. Furthermore, we will study the influence of the initial temperature perturbations on this onset age. In the last section, we will focus on the influence of the lithospheric isotherms topography on the age of first dripping instability.

In the following, we refer to the age of first dripping instability as the onset time of convection even if the concepts behind these expressions may be slightly different, as we will explain in Section 3.1.3. We also assume that the upper TBL corresponds to the lithosphere.

2 NUMERICAL SIMULATIONS OF TRANSIENT COOLING

2.1 Setup

We perform several numerical experiments to study the cooling of a hot fluid from above. The equations of conservation of mass, energy and momentum are solved in 2-D, in the Boussinesq approximation and at an infinite Prandtl number, using the code built by Christensen (1983). We neglect viscous dissipation and adiabatic heating. We normalize all variables below with the convective box height, D^*, and the internal temperature, T_i^* (see Tables 1 and 2; in the following, a star exponent denotes a dimensionalized variable). Huang *et al.* (2003) show that box aspect ratios larger than 3 do not influence the age of the first dripping instability. Therefore, we choose an aspect ratio of 4, that is sufficient to let the whole perturbation spectrum develop.

Table 1. Symbol list.

Constant	Symbol
Box height	D^*
Internal temperature	T_i^*
Thermal conductivity	k
Thermal diffusivity	K
Thermal expansion coefficient	α
Mantle density	ρ

Table 2. Variable Normalizations.

Variable	With dimension	Dimensionless
Depth	z^*	$z = \frac{z^*}{D^*}$
Time	t^*	$t = \frac{Kt^*}{D^{*2}}$
Temperature	T^*	$T = \frac{T^*}{T_i^*}$
Heat flow	q^*	$q = \frac{q^* D^*}{kT_i^*}$
Temperature drop across the sublayer	$\Delta T_{\rm ul}^*$	$\Delta T_{\rm ul} = \frac{\Delta T_{\rm ul}^*}{T_i^*}$
Height of the sublayer	δ^*	$\delta = \frac{\delta^*}{D^*}$
Radiogenic heat production	H^*	$H = \frac{H^* D^{*2}}{kT_i^*}$

The temperature is fixed at the top boundary ($T = 0$), whereas the box base and sides are insulated. The initial state is a quasi-uniform temperature field ($T = 1$), slightly perturbed in two different ways. For a first simulation series (hereafter referred to as set A), only two single punctual perturbations of less than ± 1.25 per cent are located at a depth of one third (i.e. $z = 0.333$), and at $x = 1$ and $x = 3$. For the second simulation series (hereafter referred to as set B), perturbations of random amplitude ranging from -0.1 to 0.1 per cent are spread over the whole box, on all gridpoints. Position and amplitude of the perturbations in each set are identical from one simulation to another in order to allow a comparison between the different experiments (see Section 3.2).

As the upper boundary layer cools with time, at some point, convection develops. In the analogical or numerical simulations of Davaille & Jaupart (1994) and of Choblet & Sotin (2000), the heat transferred by convection induces a cooling of the fluid below the upper TBL, no heating mode being included. Here, the fluid is internally heated to avoid any internal temperature drift and the volumetric heat production, H, is chosen to counterbalance the heat transferred by convection at thermal equilibrium. This insures that the box Rayleigh number remains constant with time. We verify that including or excluding internal heating does not modify the onset time by more than 0.3 per cent.

Viscosity in a dimensionless form is defined as

$$\nu(T) = \exp\left[-b(T-1)\right], \tag{1}$$

where b is bracketed between 9.36 and 14.80 (corresponding to a viscosity contrast across the TBL ranging from approximately

Table 3. Simulations table.

Number	Ra_i	b	H	τ_0	
				Set A	Set B
1	1.80×10^7	9.64	7.36	3.16×10^{-3}	2.89×10^{-3}
2	4.28×10^7	9.64	9.48	1.91×10^{-3}	1.62×10^{-3}
3	6.55×10^7	9.64	10.94	1.39×10^{-3}	1.24×10^{-3}
4	8.63×10^7	9.71	11.83	1.15×10^{-3}	1.05×10^{-3}
5	1.08×10^8	9.71	13.01	1.00×10^{-3}	8.96×10^{-4}
6	1.38×10^8	9.76	13.56	8.86×10^{-4}	7.66×10^{-4}
7	9.94×10^6	11.41	5.14	5.61×10^{-3}	4.75×10^{-3}
8	4.98×10^7	11.45	8.16	1.93×10^{-3}	1.68×10^{-3}
9	1.10×10^8	11.62	10.27	1.15×10^{-3}	1.03×10^{-3}
10	1.60×10^8	11.62	11.85	8.93×10^{-4}	8.00×10^{-4}
11	2.18×10^8	11.66	13.10	7.70×10^{-4}	6.56×10^{-4}
12	1.42×10^7	14.11	4.58	5.17×10^{-3}	4.42×10^{-3}
13	7.56×10^7	14.48	7.09	1.81×10^{-3}	1.52×10^{-3}
14	1.33×10^8	14.53	8.41	1.33×10^{-3}	1.04×10^{-3}
15	1.58×10^8	14.80	8.10	1.16×10^{-3}	9.54×10^{-4}
16	2.64×10^8	14.54	10.59	7.24×10^{-4}	6.76×10^{-4}
17	3.34×10^8	14.48	12.02	7.12×10^{-4}	5.80×10^{-4}
18	4.44×10^8	14.53	12.67	5.19×10^{-4}	4.84×10^{-4}

Simulations of set A have initially two single points temperature perturbations of amplitude smaller than ± 1.25 per cent and simulations of set B start with a temperature field randomly perturbed (perturbations amplitude of <0.1 per cent).

1.2×10^4 to 2.7×10^6). Despite the high viscosity temperature dependence, we choose a no-slip condition at the top of the box, first to insure that the upper part of the lithosphere will always remain rigid and secondly to allow a comparison with analogical results. An Arrhenius viscosity law would have better described the rheological behaviour of the lithosphere, yielding a higher viscous strength at low temperature. However, both rheologies are equivalent for convection beneath a rigid lid, if the parameter b in eq. (1) is taken equal to $\theta = Ea^* \Delta T^*/(RT_{\rm m}^{*2})$, where θ is the Frank-Kamenetskii parameter, Ea^* is the activation energy, $T_{\rm m}^*$ is the mantle temperature in K and R is the gas constant. $b = 15$ then corresponds to $Ea^* =$ 240 kJ mol^{-1}. Boundary conditions on the bottom and sides of the box are free slip.

All simulations are performed with a Rayleigh number Ra_i , defined as $(\alpha \rho g T_i^* D^{*3})/(K \nu_i^*)$, where α is the thermal expansion coefficient, ρ the fluid density, K the thermal diffusivity and ν_i^* is the dimensional dynamic viscosity of the fluid at T_i^* (see Table 1). It is bracketed between 9.94×10^6 and 4.44×10^8. Large Rayleigh numbers have been chosen in order to insure that convection will take place in the highly time-dependent regime (that is thought to be developing in the Earth mantle), where small-scale instabilities of the TBL are observed, and not in the stationary regime (as described in Dumoulin *et al.* 1999). Table 3 lists the Rayleigh number, Ra_i, the temperature dependence of the viscosity, b , the radiogenic heat production, H , and the obtained onset time, τ_0, for simulations sets A and B.

2.2 Onset time accuracy

The non-dimensional onset time, τ_0, is computed from the time evolution of the root mean square velocity $v_{\rm RMS}$. As shown in Fig. 1, when the first drip forms, the internal velocity rises suddenly in the fluid. Therefore, the onset time, τ_0, is calculated as the first time for which the flow acceleration, $\partial v_{\rm RMS}/\partial t$, is greater than the average velocity variation at thermal equilibrium, $\sqrt{\sum(\partial v_{\rm RMS}/\partial t)^2/N}$, N

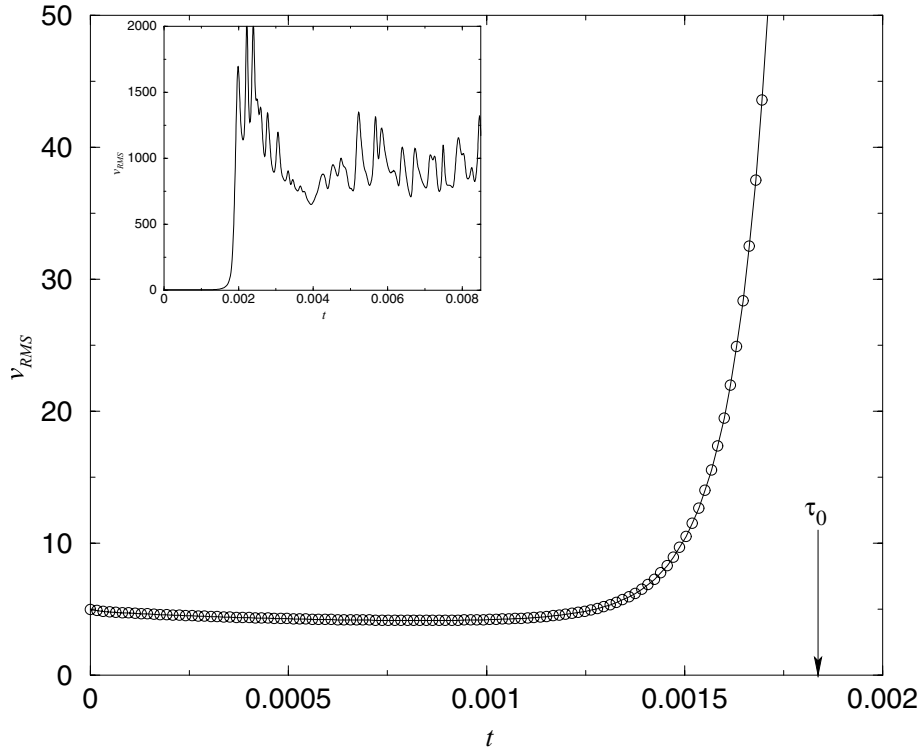

Figure 1. Time evolution of the root mean square velocity, $v_{\rm RMS}$, for simulation 13 ($Ra_i = 7.56 \times 10^7$, $b = 14.48$ and $H = 7.09$). The initial temperature field is perturbed at two single points (set A). This simulation yields an onset time of $\tau_0 = 1.81 \times 10^{-3}$. Circles are drawn at each time step. The upper left corner inset displays the velocity evolution from the beginning of the simulation to the time for which the lithosphere reaches its thermal equilibrium state.

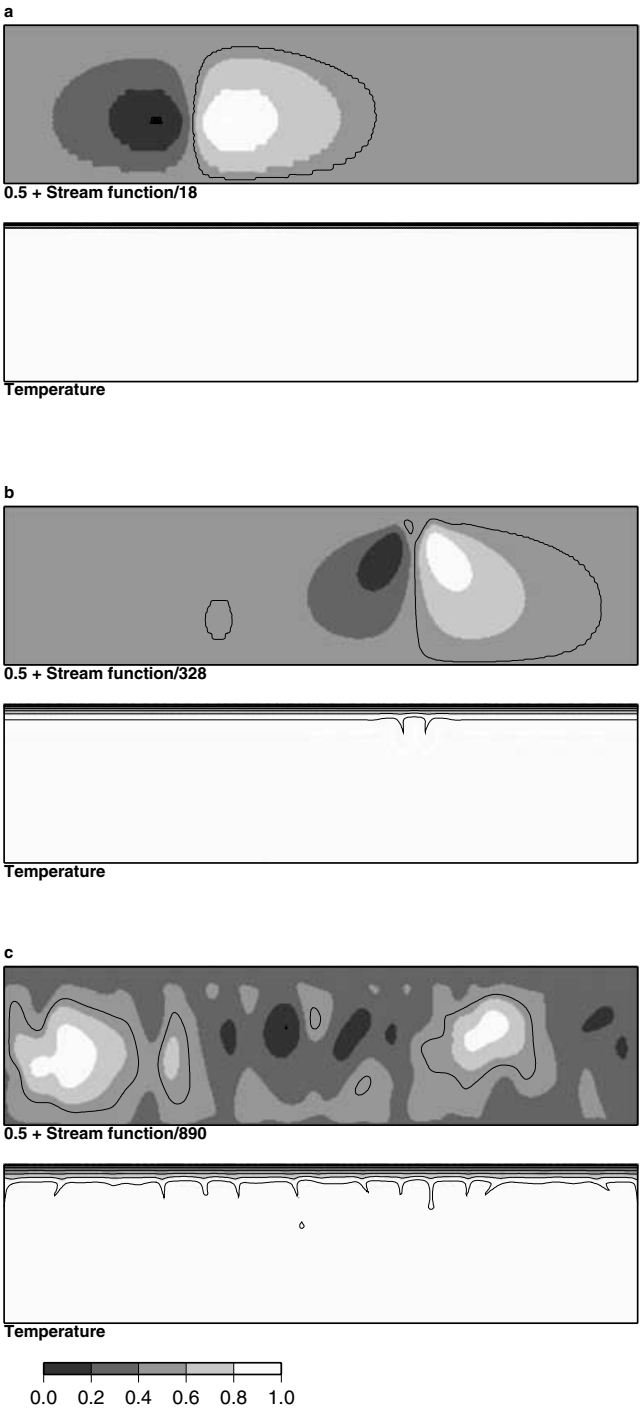

Figure 2. Stream function and temperature fields for simulation 15 of set A ($Ra_i = 1.58 \times 10^8$, $b = 14.80$ and $H = 8.10$), at (a) $t = 1.32 \times 10^{-5}$, (b) $t = 1.16 \times 10^{-3} = \tau_0$ and (c) $t = 2.64 \times 10^{-3}$. Variables are dimensionless. The stream function is normalized to be bracketed between 0.0 and 1.0. The black lines in temperature fields are isotherms.

being the number of time steps ($N > 1000$). Equilibrium is defined when parameters show quasi-static fluctuations (see insert in Fig. 1). We find empirically that our criterion is reached when the temperature profile differs by 5 per cent from that in a cooling half-space. Our estimate, τ_0, is therefore slightly larger than onset times estimated in other studies based on a 1 per cent deviation from the half-space profile.

The box is divided into 400×50 cells, with an aspect ratio of 4. In order to increase the numerical accuracy in the growing lithosphere, the grid is denser in the upper third of the box. The horizontal spacing is uniform. An accuracy test is provided for the simulation 11 of set A (see Table 3); another simulation with the same parameters is performed with a box having a 400×150 regular grid and the initial perturbations are designed to produce initial temperature structure as close as possible to the reference simulation. This new simulation has therefore the same accuracy in horizontal direction, but a more accurate precision in the vertical direction. The onset time, τ_0, is equal to 8×10^{-4} and therefore differs by 3.75 per cent from that obtained with a vertically refined 400×50 grid. Part of this difference is caused by the fact that the initial temperature perturbations distribution can not be exactly the same on the two grids, leading to a shift in the onset time (Huang *et al.* 2003).

2.3 Temporal evolution of the lithosphere thickness

Fig. 1 shows that the internal root mean square velocity is negligible for times t smaller than the onset time. The velocity at first decreases with time, then remains stable and finally, for times close to τ_0, it suddenly increases. As shown in the upper left corner inset of Fig. 1, after a maximum intensity flow driven by the appearance of the first drips, velocity decreases and reaches a statistically steady value characterizing the convection equilibrium state. The thermal structure evolves together with the mean flow velocity: when $t < \tau_0$, the lithosphere cools and thickens uniformly, maintaining flat isotherms (see Fig. 2a for a result of set A and Fig. 3a for a result of set B). At $t \simeq \tau_0$, the first instabilities appearance deflects the isotherms at the bottom of the lithosphere. It triggers large convection cells filling the whole box height below the lithosphere where an instability is about to detach, or smaller ones where instabilities just start to form, the number of cells depending on the initial temperature perturbations distribution (see Fig. 2b for set A and Fig. 3b for set B). Not much later, convection propagates and strengthens in the entire box (see Figs 2c and 3c). As already noticed in numerous previous studies (e.g. Fleitout & Yuen 1984; Davaille & Jaupart 1994), the lithosphere continues to grow even after the first instability appears and stops cooling when thermal equilibrium is reached (see Fig. 4). At thermal equilibrium, the TBL presents permanent deflections of the isotherms resulting from the interaction between the conducting lid and the instabilities triggered at the base of the TBL (Figs 2c and 3c). These deflections (bumps) allow the departure of cold material drips, the drips being fed by material sheared along the base of the TBL towards one of the bumps. The bumps amplitude and average spacing decrease with the Rayleigh number (Fig. 5).

3 FIRST DRIP DEVELOPMENT IN TRANSIENT COOLING EXPERIMENTS

3.1 Theoretical parametrization

Approximations are drawn in this section to derive a parametrization of the age of the first dripping instability, τ_0, in a fluid layer of unity height and of uniform temperature ($T = 1$). At time $t = 0$, a zero temperature is suddenly applied at the surface.

3.1.1 Unstable sublayer thickness

Because the fluid viscosity depends strongly on temperature, while cooling, a rigid lid develops at the surface, which concentrates the

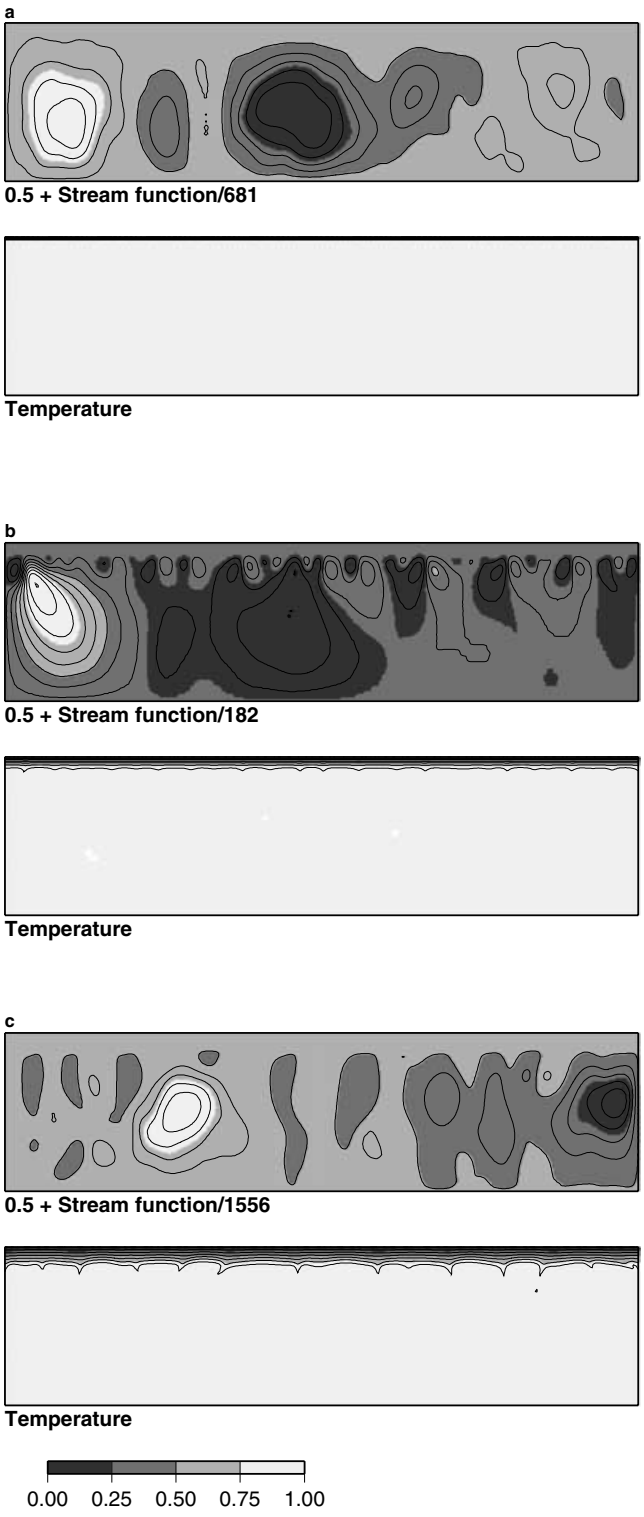

Figure 3. Stream function and temperature fields for simulation 15 of set B ($Ra_i = 1.58 \times 10^8$, $b = 14.80$ and $H = 8.10$), at (a) $t = 6.55 \times 10^{-4}$, (b) $t = 9.54 \times 10^{-4} = \tau_0$ and (c) $t = 3.84 \times 10^{-3}$. The legend is the same as for Fig. 2.

major part of the total viscosity drop across the box, exp(b). Therefore, only a thin layer at the base of the TBL is unstable, over a thickness that we approximately derive in Appendix A1. The physical bases for the chosen approximations are described below.

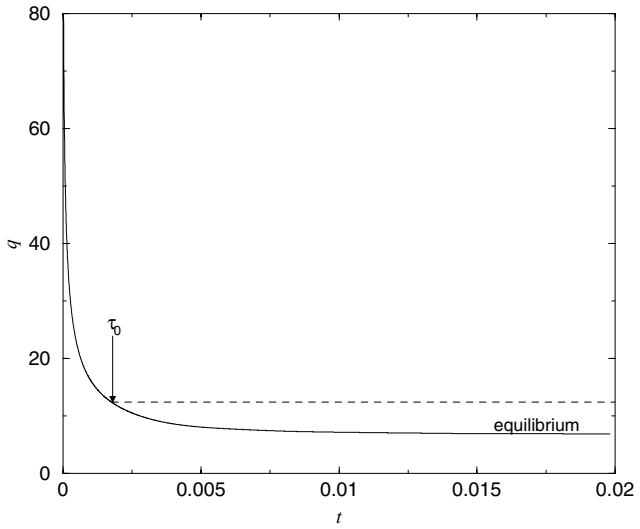

Figure 4. Time evolution of the dimensionless surface heat flow, q, for simulation 13 ($Ra_i = 7.56 \times 10^7$, $b = 14.48$, $H = 7.09$ and $\tau_0 = 1.81 \times 10^{-3}$). The initial temperature field is perturbed at two single points (set A). The dashed line represents the heat flow value at the time when the first dripping instability appears. The difference with the surface heat flow value at equilibrium shows that the lithosphere continues to cool after the onset time τ_0.

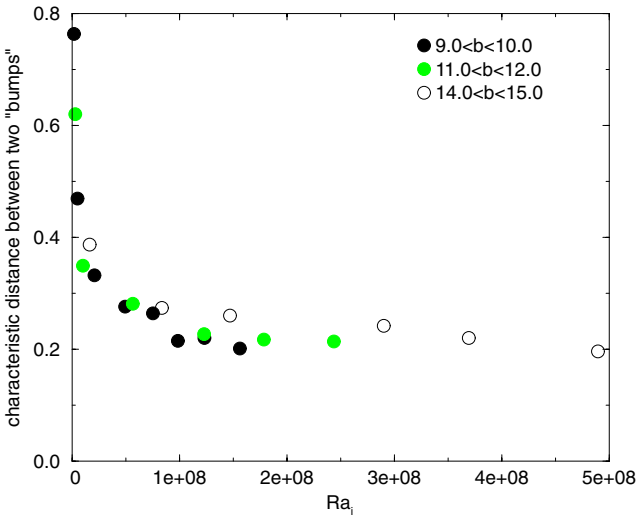

Figure 5. Characteristic distance, average through space and time, between thermal instabilities developing at the base of the lithosphere as a function of the Rayleigh number. We first locate topographic bumps on a constant basal depth level, as the segments where the temperature is lower by one standard deviation from its average value. Instability locations are then chosen in the middle of these segments. This distance can be fitted by the following relationship: $41.4\ Ra_i^{-1/3} b^{1/3}$.

We let d_{rl} be the rigid lid thickness at $t = \tau_0$. We consider that the unstable sublayer, starts from the depth d_{rl} and extends downwards until the depth at which $T = 1$ (see Fig. 6). We therefore limit the sublayer to the area with non-zero temperature gradients, i.e. to the area where temperature anomalies will develop preferentially. In other words, we assume that the main destabilization mode is confined to the TBL and therefore that it has a horizontal wavelength of the order of the sublayer thickness. However, we should bear in mind that, although the first developing thermal heterogeneity

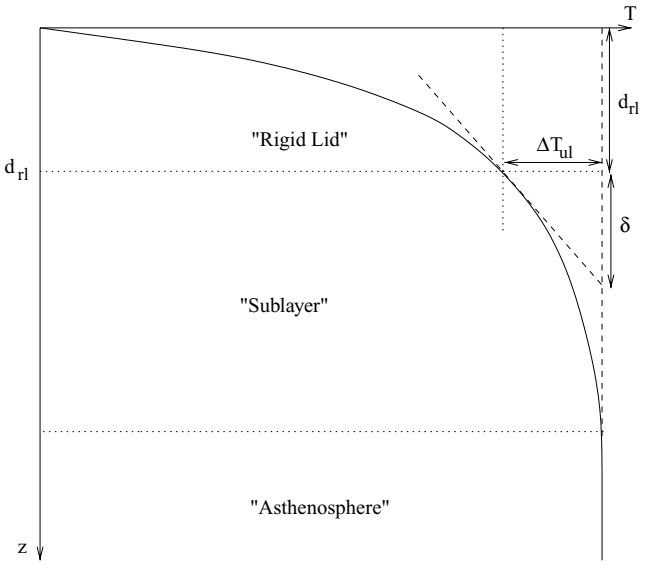

Figure 6. Sketch representing the assumed temperature structure of the cooling thermal boundary layer (TBL) for ages smaller than the age of the first dripping instability.

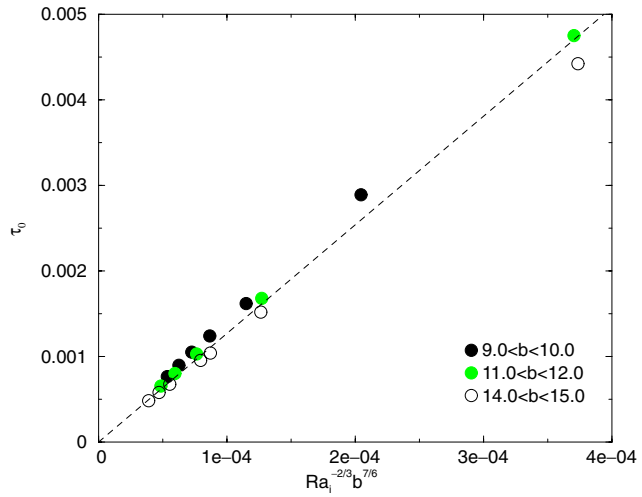

Figure 7. Age of first dripping instability obtained for set B , τ_0, is plotted as a function of $Ra_i^{-2/3}b^{7/6}$. This scaling is obtained with the assumption that marginal stability controls τ_0. Black circles are drawn for simulations with $9.0 < b < 10.0$, grey circles for simulations with $11.0 < b < 12.0$ and open circles for simulations with $14.0 < b < 15.0$. A linear regression (dashed line) yields a slope of 12.70.

remains confined to the TBL, its associated velocity field develops in the whole box.

The temperature drop across the unstable layer, $\Delta T_{\rm ul} = 2.23\, b^{-1}$, is such that the fluid in the sublayer can be approximately considered as isoviscous, with the fluid viscosity at $T = 1$. The sublayer thickness is thus controlled by the temperature structure. Because of very low flow velocities, we can safely assume that, until the first thermal instability is detected, the fluid cools by conduction alone in a homogeneous half-space. The temperature structure therefore follows the erf function for ages smaller than τ_0. The sublayer thickness, δ, is then obtained by the straight continuation of the temperature gradient at $z = d_{\rm rl}$ (defined by $T\ (d_{\rm rl}) = 1 - \Delta T_{\rm ul}$). It is important to note that δ is an approximation of the sublayer thickness and that it is always underevaluated.

Based on these assumptions, the analysis detailed in Appendix(A1) yields

$$\delta \simeq 0.83\sqrt{\pi} b^{-1/4}\sqrt{\tau_0}. \qquad (2)$$

With this estimation of the sublayer thickness at $t = \tau_0$, it is possible to parametrize the age of the first dripping instability. However, note that this thickness corresponds to that of a theoretical equivalent sublayer both isoviscous and with a linear temperature profile, and that it only approaches the true sublayer thickness. Furthermore, the boundary conditions that will be applied to this theoretical sublayer are constant temperatures with no slip at its surface and with free slip at its base.

3.1.2 The marginal stability analysis

The usual approach (Davaille & Jaupart 1994; Choblet & Sotin 2000; Korenaga & Jordan 2003) consists of assuming that the first TBL instability drips when the TBL reaches its marginal stability state, i.e. when the local Rayleigh number (defined with the TBL thickness and the temperature drop across it) is equal to a critical Rayleigh number. The analysis classically focuses on the theoretical isoviscous sublayer presented above. If we assume that the first instability appears when the sublayer is marginally stable (i.e. when the Rayleigh number of the sublayer, $Ra_{\rm ul}$, is equal to the critical Rayleigh number for an isoviscous fluid, $Ra_{\rm cr-is}$), it implies the following.

(i) For ages smaller than τ_0 the system is stable. All perturbations have negative growth rates or, if positive, growth rates are small enough for them to be inhibited by the growth of the top TBL.

(ii) At $t = \tau_0$, the growth rate of a perturbation in the isoviscous sublayer is equal to 0.

(iii) When $t = \tau_0 + \epsilon$, with ϵ very small compared with τ_0, the growth rate of a thermal perturbation in the isoviscous sublayer is large enough for the first dripping instability to be fully developed.

Based on these principles, the analysis described in Appendix A2 yields the following parametrization for τ_0 :

$$\tau_0 \simeq 0.85\frac{Ra_{\rm cr-is}^{2/3}}{\pi} Ra_i^{-2/3} b^{7/6}. \qquad (3)$$

This parametrization is tested with the values of τ_0 obtained for sets A and B as a function of $Ra_i^{-2/3}b^{7/6}$ (Fig. 7 shows results for set B). The linear correlation coefficient and the slope are equal to 0.9955 and 14.77, respectively, for set A , while they are equal to 0.9952 and 12.70, respectively, for set B . The assumption $Ra_{\rm ul} = Ra_{\rm cr-is}$ used in eq. (3) yields a critical isoviscous Rayleigh number of approximately 403 (set A) or 322 (set B), in good agreement with the value of 505 obtained for an isoviscous layer and a rigid/half-space boundary condition (see Appendix B). In Fig. 7, different symbols represent increasing temperature viscosity contrasts. They show a small but systematic drift in the τ_0 –Ra_i relationship as a function of b . The expression obtained with the same approach by Choblet & Sotin (2000; $\tau_0 \propto Ra_i^{-2/3}b^{8/3}$) is slightly different because they did not take into account the sublayer thickness dependence on the viscosity contrast exp (b) that is given by eq. (2). Our results, expressed as a function of their scaling law, show therefore a strong scatter depending on the range of b (Fig. 8 shows results for set B). This was already noted by Huang *et al.* (2003) and Korenaga & Jordan (2003), who observed that the b exponent of the viscosity temperature dependence in the onset time parametrization should be smaller than what Davaille & Jaupart (1994) and Choblet & Sotin (2000) proposed.

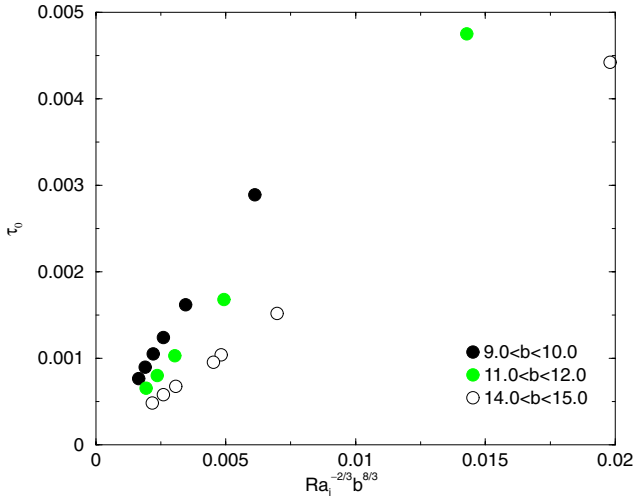

Figure 8. The age of first dripping instability, τ_0, obtained for set B , is plotted as a function of $Ra_i^{-2/3}b^{8/3}$. This scaling is obtained by Choblet & Sotin (2000), with the assumptions that marginal stability controls τ_0 and that viscosity contrasts are small. Black circles correspond to simulations with $9.0 < b < 10.0$, grey circles to simulations with $11.0 < b < 12.0$ and open circles to simulations with $14.0 < b < 15.0$. Note that τ_0 displays a systematic offset as a function of the viscosity contrast exp (b).

3.1.3 Growth rate of thermal instabilities

Another approach to parametrize τ_0 is to assume that the temporal evolution of perturbation growth rates controls the development of the first dripping instability (Yuen & Fleitout 1984) and therefore τ_0 ; this implies the following.

(i) At time $\tau_1 \ll \tau_0$, there is at least one perturbation in the whole fluid layer with a growth rate equal to 0. τ_1 is the true convection onset time in the box.

(ii) The positive growth rates of the perturbations are initially (for t close to τ_1) very small and they increase only slowly with age.

(iii) At $t = \tau_0$, the cumulated development of perturbation is large enough for an instability to be detected. We therefore assume that the sublayer local Rayleigh number Ra_{ul} is much greater than the isoviscous critical Rayleigh number $Ra_{\mathrm{cr-is}}$ at $t = \tau_0$. Note that, in this context, the term onset time for τ_0 is not appropriate.

The parametrization of τ_0 following this hypothesis yields (Appendix A3)

$$\tau_0 \propto Ra_i^{-2/3} b^{5/6}. \quad (4)$$

Fig. 9 presents the obtained relationship if we assume that the growth rates of thermal perturbations control the appearance age of the first dripping instability. The linear correlation coefficient and the regression slope between the obtained τ_0 and $Ra_i^{-2/3}b^{5/6}$ are equal to 0.9990 and 33.93, respectively, for set A , while they are equal to 0.9997 and 29.20, respectively, for set B .

Korenaga & Jordan (2003) derived a parametrization of the onset time valid for small and large viscosity contrasts, assuming the marginal stability of the lithosphere and using a local Rayleigh number defined with the lithospheric buoyancy weighted by the viscosity. Their scaling law is displayed on Fig. 10 together with the two scaling laws derived in the present study (eqs 3 and 4) and our numerical results. The latter suggest that the exponent of the viscosity dependence, b , is slightly overestimated by both scaling laws based on the marginal stability assumption. This is confirmed by the slope as a function of b defined by the results of Korenaga & Jordan (2003;

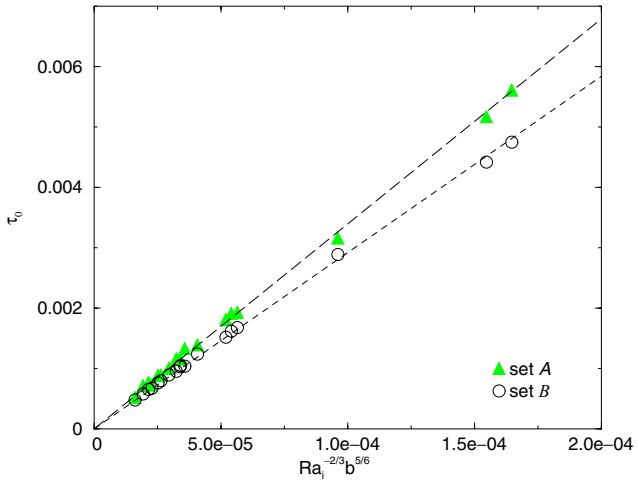

Figure 9. The age of first dripping instability, τ_0, is plotted as a function of $Ra_i^{-2/3}b^{5/6}$. This scaling is obtained with the assumption that perturbations growth rates control τ_0. Grey triangles are drawn for simulations with two initial single point perturbations (set A) and circles for simulations having an initial temperature field randomly perturbed (set B). The regression slopes are respectively of 33.93 and 29.20.

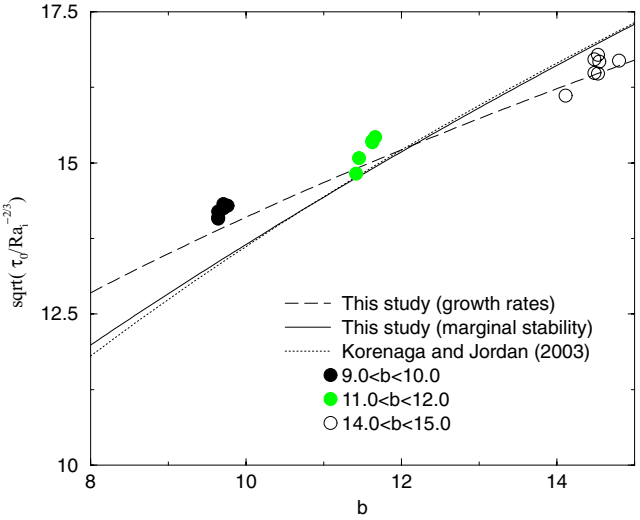

Figure 10. $\sqrt{\tau_0/Ra_i^{-2/3}}$ is plotted as a function of the temperature dependence of the viscosity b . Our simulation results for set B are shown with circles. The dotted line represents Korenaga & Jordan (2003) parametrization of τ_0 based on the assumption of the marginal stability of the lithosphere at the onset time. Solid and dashed lines represent the scaling laws derived in this study based on the marginal stability (eq. 3) and on the temporal evolution of perturbations growth rates (eq. 4), respectively.

as shown in fig. 5 of their article), which is also slightly smaller than predicted by their scaling law.

3.2 Influence of the initial state

Huang *et al.* (2003) and Korenaga & Jordan (2003) have shown that larger amplitude perturbations trigger the first dripping instability earlier than smaller amplitude perturbations. This is not in contradiction with our results for sets A and B : ages of first dripping instability obtained for set B (random temperature anomalies of less than ± 0.1 per cent spread over the whole box) are always

smaller than the ones obtained for set *A* (two punctual temperature anomalies of ±1.25 per cent). The earlier onset for set *A* with respect to set *B* expresses the fact that, although thermal perturbations induce instantaneously a velocity field spread into the whole box, velocity amplitudes at the base of the TBL depend not only on the perturbations amplitude but also on their location and structure (i.e. wavelength).

To further analyse the influence of the initial temperature state on the age of the first dripping instability, we perform a few other simulations with various temperature perturbations and a single set of convection parameters (simulation 8: $Ra_i = 4.98 \times 10^7$, $b = 11.45$ and $H = 8.16$). In one simulation, the initial temperature field is extracted from the core region of a fully convecting box, from which the upper TBL has been deleted. Therefore, the initial thermal anomalies are in this case of finite amplitude (in contrast to the studies of Huang *et al.* 2003, and Korenaga & Jordan 2003). The initial temperature heterogeneities, that were present mainly in the form of downgoing droplets in a quite homogeneous matrix, first sink into the box, diffuse and progressively disappear. As thermal anomalies are not regenerated in the upper TBL, the internal velocity decreases. During that time, the top boundary layer develops uniformly by cooling from its initially infinitely thin thickness, maintaining flat isotherms. The internal velocity rises for the first time when the first dripping instability appears. We note that the delay between cooling initiation and the first dripping instability ($\tau = 7.2 \times 10^{-4}$) is more than two times lower in this case than the one obtained for sets *A* ($\tau_0 = 1.93 \times 10^{-3}$) and *B* ($\tau_0 = 1.68 \times 10^{-3}$), but still non-negligible. Therefore, the finite amplitude initial perturbations present in the box cannot immediately trigger an instability of the upper TBL, however they significantly decrease the time at which it occurs.

To further constrain the conditions triggering the first instability development, we also perform a simulation in which the initial temperature structure already results from the conductive cooling of an infinite half-space at time $t_{\rm erf}$, i.e. $T(z) = \mathrm{erf}(z/2\sqrt{t_{\rm erf}})$. $t_{\rm erf}$ is chosen as the age of the first dripping instability (τ_0) inferred from the corresponding simulation of set *A* . The marginal stability of the TBL is therefore already assumed from the beginning of this simulation. However, we find in this case that the age of first dripping instability ($\tau_0^{\rm erf} = 8.28 \times 10^{-4}$) is only a factor 2 smaller than $t_{\rm erf}$ and is not negligible. Consequently, even if the sublayer Rayleigh number is reaching the isoviscous critical Rayleigh number at τ_0, growth rates of thermal perturbations do not suddenly become very large.

3.3 Discussion

In Section 3.1, two different parametrizations for the onset time in a fluid cooled from above have been derived, based on a marginal stability analysis and on perturbation growth rates. The second parametrization slightly better adjusts our results than the first one. Furthermore, simulations with different initial temperature perturbations or boundary layer thermal structures (Section 3.2) show that growth rates play an important role in controlling the onset times. On the other hand, the fact that the calculated local Rayleigh number characterizing the unstable sublayer, $Ra_{\rm ul}$ (as defined in Section 3.1 and in Appendix A), of about 400, is close to the isoviscous critical Rayleigh number at onset time is probably not a coincidence.

However, we emphasize that this theoretical approach is an idealized and simplified representation of the physical system, based on two main simplifications: (i) the unstable sublayer thickness δ is always strongly underestimated; (ii) the unstable sublayer is supposed to be isoviscous and the temperature profile through it linear. A numerical linear stability analysis (performed with the code described in Appendix B) on the complete system allows to better define, at τ_0, the ratio between the Rayleigh number of a given layer (Ra_l , calculated with the true layer thickness) and the critical Rayleigh number of this same layer ($Ra_{\rm cr}$, calculated with the true layer temperature and viscosity profiles) at τ_0. An example of calculations is applied to the exact temperature and viscosity profiles obtained in simulation 8 (set *A*) at the onset time and considering different layers. As shown on Fig. 11, the Rayleigh number defined on the entire box is, at the onset time, much larger than the critical Rayleigh number calculated for the same layer. This means that some perturbations have positive growth rates at times smaller than τ_0, perturbations that are not restricted to the sublayer. The fact that the two former simplified analyses seem to represent well the numerical results indicates that

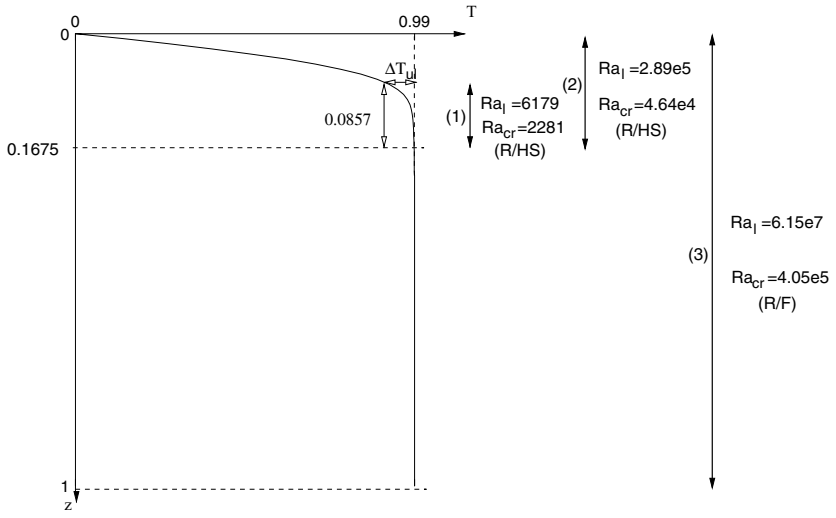

Figure 11. Temperature profile obtained at the onset time τ_0 for simulation 8 of set *A* . Critical Rayleigh numbers ($Ra_{\rm cr}$) have been computed with the code described in Appendix B, for the displayed non-linear temperature profile, and for three layers of increasing sizes: (1) the unstable sublayer, (2) the upper thermal boundary layer (TBL) and (3) the whole box. Boundary conditions used, respectively, for the upper and lower surfaces are given between parentheses: R (rigid), F (free), or HS (half-space). Local Rayleigh numbers are also given for each layer (Ra_l). Ra_l and $Ra_{\rm cr}$ are based on the bottom layer viscosity.

these perturbations do not affect the lithospheric isotherms sufficiently to trigger a dripping instability. On the other hand, at τ_0, the local Rayleigh number defined for the entire TBL is greater by a factor 6 than the TBL critical Rayleigh number. Zooming further in, the local Rayleigh number of the unstable sublayer (defined with its true thickness) is larger by a factor 3 than the sublayer critical Rayleigh number. The latter critical Rayleigh number is overestimated because a rigid boundary condition with no temperature perturbation is applied to the sublayer surface. These conditions are not realistic for a sublayer with a viscosity contrast of only exp (2.23) (see a demonstration in Stengel *et al.* 1982). We therefore retain the ratio Ra_l/Ra_{cr} of 6 at onset time, obtained for the whole TBL. This ratio is neither very large (growth rate analysis assumption), nor equal to 1 (marginal stability assumption). From that, we conclude that both perturbation growth rates and marginal stability must be taken into account to describe the first drip development. However, all approaches developed above are based on only one deformation mode centred on an isolated boundary layer. Mode interactions cannot be taken into account in such simplified approaches.

4 INFLUENCE OF THE LITHOSPHERIC ISOTHERMS TOPOGRAPHY ON THE AGE OF THE FIRST DRIPPING INSTABILITY

The previous study cannot apply directly to the oceanic lithosphere, because the latter is never a flat TBL in the two horizontal directions. A permanent isotherm topography results from transform faults and from lithospheric progressive thickening away from ridges. In this section, we address the question of how this topography influences the age of the first dripping instability.

4.1 Influence of transform faults

We study the influence of transform faults, through a simulation in which two different TBL structures initially coexist across a transform fault (Fig. 12a). On the left side, the initial thermal structure follows an erf function with a lithospheric age $t_{erf} = \tau_0$, while on the right side, the lithosphere has a null age. Temperature perturbations have the same amplitude and location as those described in Section 2.1 for set A . The parameters used for this simulation are again $Ra_i = 4.98 \times 10^7$, $b = 11.45$ and $H = 8.16$ (as in Section 3.2). The transform fault yields finite horizontal temperature gradients in the TBL, a situation that is always unstable. Therefore, a thermal dripping instability is expected in the early simulation stage beneath the transform fault. Indeed, the first drip appears at the junction between the two different lithospheres (Fig. 12b) at a time $t = \tau_0' = 1.92 \times 10^{-4}$ much smaller than the ages τ_0 and τ_0^{erf} reported for each separated initial states (see Section 3.2). The second drip appears on the left side of the transform fault at $t = \tau_2 = 8 \times 10^{-4}$ (Fig. 12c). This age is only slightly smaller than τ_0^{erf} obtained with a uniform initial temperature structure of age $t_{erf} = \tau_0$. Finally, small-scale convection, well developed on the left side, propagates on the right side at an age $t = \tau_3 = 1.9 \times 10^{-3}$, close to τ_0. τ_0' and τ_2 correspond to a marked increase in the internal velocity field, whereas the small-scale convection onset on the right side is masked in the average velocity time evolution by an already well-developed flow (see Fig. 13). Note that Huang *et al.* (2003) found similar results with lithospheres of smaller ages t_{erf}.

In conclusion, the topography of the lithosphere, as soon as it is sharp, plays a preponderant role in the age of the first lithospheric drip.

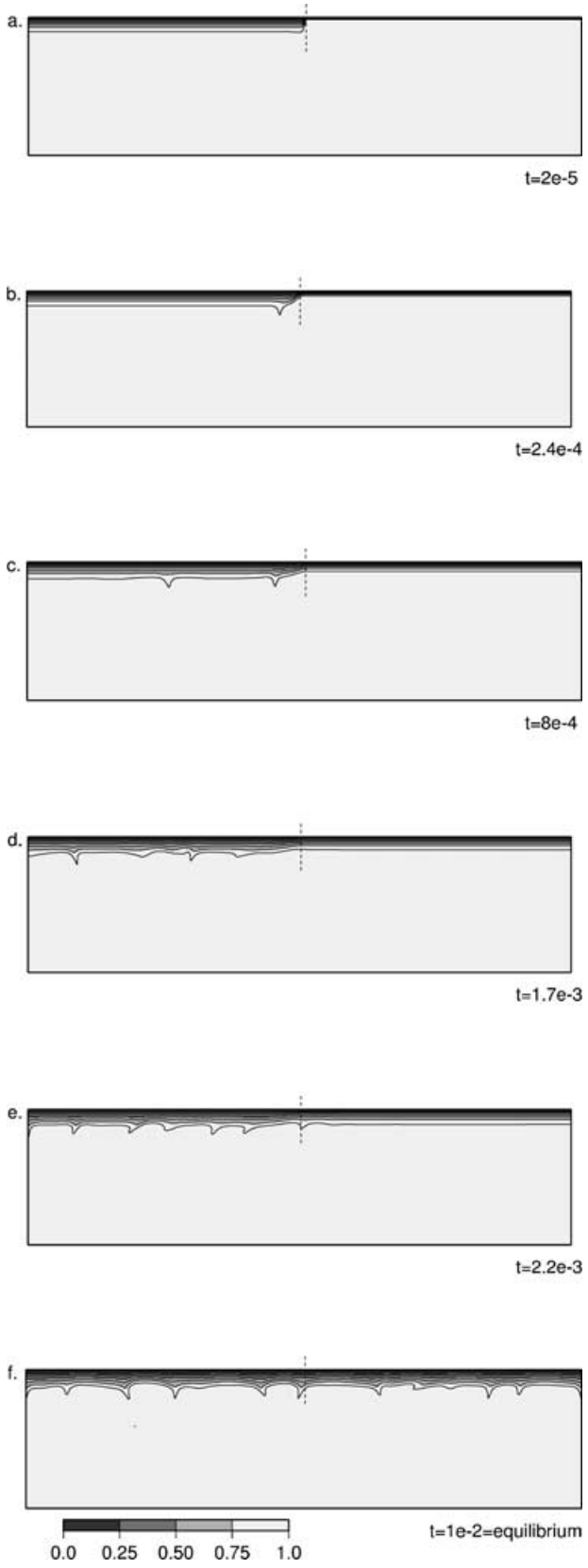

Figure 12. Temperature fields at different times obtained for the simulation with a transform fault: (a) the initial temperature field (a lithosphere of age $t_{erf} = \tau_0$ on the left side and of age $t = 0$ on the right side), (b) at $\tau_0' < t < \tau_2$, (c) at $t = \tau_2$, (d) at $\tau_2 < t < \tau_3$, (e) at $t > \tau_3$, and (f) at thermal equilibrium ($t \gg \tau_3$).

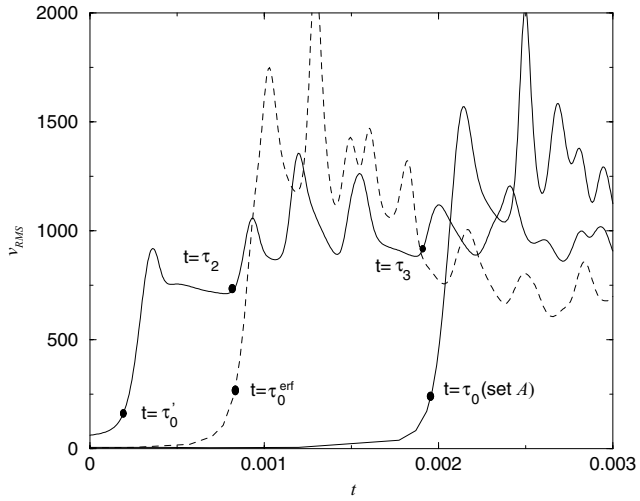

Figure 13. Time evolution of the root mean square velocity, v_{RMS}, for three simulations with parameters of simulation 8 (set A): $Ra_i = 4.98 \times 10^7$, $b = 11.45$ and $H = 8.16$. At t = 0, two lithospheres of different ages coexist across a transform fault: a lithosphere of age $t_{\mathrm{erf}} = \tau_0 = 1.93 \times 10^{-3}$ on the left side and a lithosphere of age $t = 0$ on the right side of the box (thick black line). See also temperature evolution in Fig. 12. For comparison, the dashed and thin solid lines are drawn for an initial uniform state having lithosphere of age $t_{\mathrm{erf}} = \tau_0$ and of age $t = 0$, respectively.

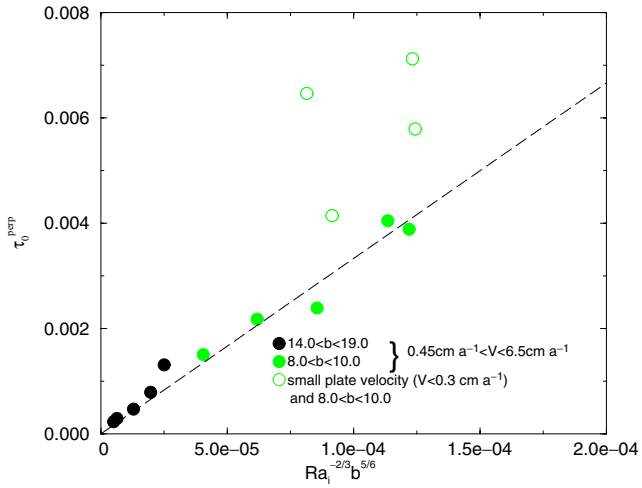

Figure 15. Age of the first dripping instability obtained in simulations of lithospheric cooling perpendicularly to the ridge, τ_0^{perp}, is plotted as a function of $Ra_i^{-2/3}b^{5/6}$. This scaling is obtained with the assumption that perturbation growth rates control the age of the first dripping instability. Grey circles are pictured for simulations with $8.0 < b < 10.0$, black circles for simulations with $14.0 < b < 19.0$. Open circles are indicating four points with very low plate velocities V . The linear regression (dashed line), which excludes points with very low plate velocities, yields a slope of 33.3, close to the previously calculated ones (see Fig. 9)

4.2 Influence of the ridge topography

In order to study the influence of the isotherm topography close to the ridge on the age of the first dripping instability, we use previous simulations of 2-D lithospheric cooling away from a ridge presented in Dumoulin *et al.* (2001). These simulations have a rheology similar to the one presented in Section 2, or are new runs performed with an Arrhenius rheology. All experiments are internally heated and the viscosity depends both on temperature and pressure. In these simulations (Fig. 14), a first drip develops at some distance from the ridge and is advected away from the ridge together with plate motion. After sometime, a new drip appears between the former first drip and the ridge. This cycle is repeated indefinitely. Further away from the ridge, the lithosphere isotherms present pronounced bumps or corrugations, advected with plate motion and from which drips depart.

The average distance between this drip and the ridge is found using a criterion based on the temporal variability of the lithospheric thickness, that is defined by a basal isotherm. This distance is then transformed into lithospheric age using the surface velocity. On Fig. 15, the age of the first dripping instability τ_0^{erf} is represented versus $Ra_i^{-2/3}b^{5/6}$, that is the scaling law based on the perturbation growth rates. Note that because the first developing drips are successively advected away from the ridge, the uncertainty on their average location is large, resulting in less accuracy than in the transient cooling study.

Fig. 15 shows that the scaling law for the age of the first dripping instability also applies when the lithospheric base has a topography close to the ridge. Four points corresponding to simulations with very low surface velocities do not follow the scaling law. In these cases, the scaling law predicts that the drip should appear very close to the ridge, closer than it does in our simulations. However, the asthenospheric flow rising up below the ridge probably prevents the downgoing flow associated with the drip to occur too close from the ridge. It therefore delays the age of the first drip. In Dumoulin *et al.* (2001), we noted that, close to the ridge, cold material was flowing inside the lithosphere base and was feeding the first drip. This flow, taking place along a smooth topography, seems to have no consequence on the age of the first dripping instability.

In the cases presented here, although performed in 2-D, the shearing resulting from plate motion and asthenospheric flow does not

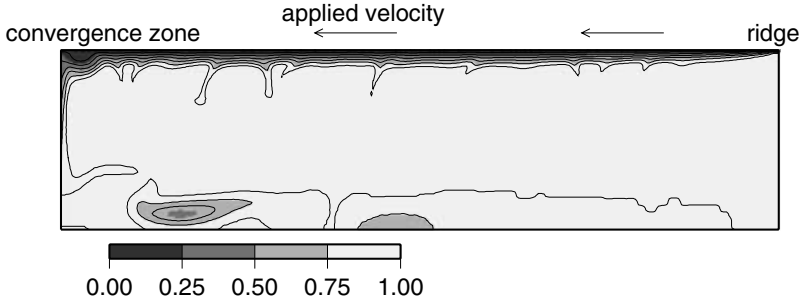

Figure 14. Example of a temperature field obtained for a simulation with a constant velocity applied at its surface, from a ridge to a convergence zone (see Dumoulin *et al.* 2001).

seem to delay the onset of small-scale convection. Van Hunen *et al.* (2003) studied the effect of the shearing resulting from a moving plate on the onset of small-scale convection for various box geometries (2-D or 3-D). They showed that, in 2-D, onset times are delayed for plate velocities (or the Peclet number) exceeding a threshold, that increases with the Rayleigh number. Our simulations are performed at lower Peclet/Rayleigh ratios than the ones described in Van Hunen *et al.* (2003). It is therefore not surprising that 2-D shearing here does not influence the onset times. In 3-D, shearing does not affect onset times, however its influence on the instability geometry depends on the Peclet/Rayleigh ratio (Van Hunen *et al.* 2003).

5 CONCLUSION

In order to study the onset of small-scale convection τ_0 under cooling lithospheres, we performed 2-D simulations of the cooling of a hot fluid from above. Because of the strong temperature dependence of the fluid viscosity, a conductive lid forms at the surface during the cooling and, at $t = \tau_0$, a cold drip departs from the base of this upper boundary layer. The main results we obtain are listed below.

(i) We derive two new scaling laws for τ_0. The first is based on the usual assumption that, at $t = \tau_0$, the upper boundary layer is in a marginal stability state. It yields

$$\tau_0 \simeq 14 Ra_i^{-2/3} b^{7/6}.$$

This relationship takes into account the strong temperature dependence of viscosity, contrary to Davaille & Jaupart (1993) and Choblet & Sotin (2000). This leads to a different exponent in b .

The second scaling law is based on the assumption that the age of first dripping instability is controlled by the temporal evolution of perturbation growth rates:

$$\tau_0 \simeq 31 Ra_i^{-2/3} b^{5/6}.$$

Both scaling laws are consistent with our numerical results, those of Huang *et al.* (2003) and those of Korenaga & Jordan (2003). However, the slightly lower b exponent in the second relationship is in better agreement with our results and those of Korenaga & Jordan (2003).

(ii) These scaling laws yield a dimensionalized onset time that does not depends on the box height. Furthermore, because the uncertainty on asthenospheric viscosity is much larger than that on activation energy, the computed dimensionalized onset time will depend more on the chosen viscosity than on the chosen activation energy. For an asthenospheric viscosity ranging from 2×10^{18} to 5×10^{19} Pa s the onset time of small-scale convection varies from 12–17 to 102–147 Myr (depending on the activation energy: 240 to 300 kJ mol^{-1}), respectively. Therefore, continental lithosphere should undergo small-scale convection at their base, sometime (<150 Ma) after their thermal rejuvenation (stretching episodes or orogenic collapses). Furthermore, some sharp basal topography of the continental lithosphere is likely to be inherited from former tectonic events. As shown here, it will strongly promote the early triggering of small-scale convective movements. The case of oceanic lithospheres is more controversial because they disappear by subduction before 180 Myr. The exact choice of the asthenospheric viscosity will therefore control the expected flow beneath the oceanic lithosphere and its cooling mode. Transform fault spacing will also be a key parameter.

(iii) The importance of growth rates in controlling τ_0 is underlined by simulations having different initial temperature perturbations (in amplitude and location) and by simulations having an already thickened upper boundary layer at $t = 0$. For example, a lithosphere defined initially with a half-space temperature structure at τ_0, which therefore could be assumed to be in marginal state, will not be destabilized immediately, but after a time non-negligible compared with τ_0.

(iv) Because of its finite growth rates, small-scale convection should appear earlier than predicted by the eqs (3) and (4) below the oceanic lithosphere. Small-scale convection age should depend on the amplitude of thermal perturbations within the core mantle flow and on the inherited lithospheric base topography. The influence of the latter on the onset time of small-scale convection is twofold: (a) a sharp topography (induced for example by transform faults) will produce the departure of a cold drip at a time much smaller than τ_0; (b) on the other hand, for the smooth topography induced by lithospheric cooling, the first cold drip develops for a lithospheric age consistent with the laws derived for transient cooling cases. In conclusion, we expect that small-scale convection will develop at an age consistent (by approximately 20 per cent) with that given above far from fracture zones and significantly earlier below fracture zones (depending on the age offset). A 3-D study should constrain the flow geometry (large and small scale) in the presence of both transform faults and lithospheric cooling from the ridge. Some phenomena, like partial melting, may also trigger earlier the small-scale convection.

ACKNOWLEDGMENTS

We thank Jeroen Van Hunen and an anonymous reviewer for their useful comments and careful reviews. This work was supported by the French Ministry of Research and CNRS.

REFERENCES

Buck, W.R., 1985. When does small scale convection begin beneath oceanic lithosphere?, *Nature,* **313,** 775–77.

Buffett, B.A., Gable, C.W. & O'Connell, R.J., 1994. Linear stability of a layered fluid with mobile surface plates, *J. geophys. Res.,* **99,** 19 885–19 900.

Choblet, G. & Sotin, C., 2000. 3D thermal convection with variable viscosity: can transient cooling be described by a quasi-static scaling law?, *Phys. Earth planet. Int.,* **119,** 321–336.

Christensen, U.R., 1983. Convection in a variable-viscosity fluid: Newtonian versus power-law rheology, *Earth planet. Sci. Lett.,* **64,** 153–162.

Colin, P. & Fleitout, L., 1990. Topography of the ocean floor: thermal evolution of the lithosphere and interaction of deep mantle heterogeneities with the lithosphere, *Geophys. Res. Lett.,* **17,** 1961–1964.

Davaille, A. & Jaupart, C., 1993. Transient high-Rayleigh-number thermal convection with large viscosity variations, *J. Fluid Mech.,* **253,** 141–166.

Davaille, A. & Jaupart, C., 1994. Onset of thermal convection in fluids with temperature-dependent viscosity: application to the oceanic mantle, *J. geophys. Res.,* **99,** 19 853–19 866.

Doin, M.P. & Fleitout, L., 1996. Thermal evolution of the oceanic lithosphere: An alternative view, *Earth planet. Sci. Lett.,* **142,** 121–136.

Dumoulin, C., 2000. Convection mantellique et structure thermique de la lithosphère, *PhD thesis,* Univ. Paris XI, Paris.

Dumoulin, C., Doin, M.P. & Fleitout, L., 1999. Heat transport in stagnant lid convection with temperature- and pressure-dependent newtonian or non-newtonian rheology, *J. geophys. Res.,* **104,** 12 759–12 778.

Dumoulin, C., Doin, M.P. & Fleitout, L., 2001. Numerical simulations of the cooling of an oceanic lithosphere above a convective mantle, *Phys. Earth planet. Int.,* **125,** 45–64.

Fleitout, L. & Yuen, D., 1984. Secondary convection and the growth of oceanic lithosphere, *Phys. Earth planet. Inter.,* **36,** 181–212.
Grasset, O. & Parmentier, E.M., 1998. Thermal convection in a volumetrically heated, infinite Prandtl number fluid with strongly temperature-dependent viscosity. Implications for planetary thermal evolution, *J. geophys. Res.,* **103,** 18 171–18 181.
Haxby, W.F. & Weissel, J.K., 1986. Evidence for small-scale convection from seasat altimeter data, *J. geophys. Res.,* **91,** 3507–3520.
Howard, L.N., 1964. Convection at high Rayleigh number. In: ed. Gortler H., pp. 1109–1115 *Proceedings of the 11th International Congress on Applied Mechanics,* Springer-Verlag, New York.
Huang, J., Zhong, S. & Van Hunen, J., 2003. Controls on sublithospheric small-scale convection, *J. geophys. Res.,* **108,** 2405–2417.
Korenaga, J. & Jordan, T.H., 2003. Physics of multi-scale convection in the Earth's mantle 1. Onset of sublithospheric convection, *J. geophys. Res.,* **108**(B7), 2333, doi:10.1029/2002JB001760.
Montagner, J.-P., 2002. Upper mantle low anisotropy channels below the Pacific Plate, *Earth planet. Sci. Lett.,* **202,** 263–274.
Morris, S. & Canright, D., 1984. A boundary-layer analysis of Bénard convection in a fluid of strongly temperature-dependent viscosity, *Phys. Earth planet. Int.,* **36,** 355–373.
Parsons, B. & Sclater, J.G., 1977. An analysis of the variation of ocean floor bathymetry and heat flow with age, *J. geophys. Res.,* **82,** 803–827.
Reese, C., Solomatov, V., Baumgardner, J. & Yang, W., 1999. Stagnant lid convection in a spherical shell, *Phys. Earth planet. Int.,* **116,** 1–7.
Richter, F.M. & Parsons, B., 1975. On the interaction of two scales of mantle convection, *J. geophys. Res.,* **80,** 2529–2541.
Solomatov, V.S., 1995. Scaling of temperature- and stress-dependent viscosity convection, *Phys. Fluids,* **7,** 266–274.
Solomatov, V.S. & Moresi, L.N., 2000. Scaling of time-dependent stagnant lid convection: Application to small-scale convection on earth and other terrestrial planets, *J. geophys. Res.,* **105,** 21 795–21 817.
Stein, C.A. & Stein, S., 1992. A model for the global variation in oceanic depth and heat flow with lithospheric age, *Nature,* **359,** 123–129.
Stengel, K.C., Oliver, D.S. & Booker, J.R., 1982. Onset of convection in a variable viscosity fluid, *J. Fluid Mech.,* **120,** 411–431.
Turcotte, D.L. & Schubert, G., 1982. *Geodynamics: Applications of Continuum Physics to Geological Problems,* Wiley, New York.
Van Hunen, J., Huang, J. & Zhong, S., 2003. The effect of shearing on the onset and vigor of small-scale convection in a Newtonian rheology, *Geophys. Res. Lett.,* **30**(19), 1991, doi:10.1029/2003GL018101.
Yuen, D.A. & Fleitout, L., 1984. Stability of the oceanic lithosphere with variable viscosity: an initial-value approach, *Phys. Earth planet. Int.,* **343,** 173–185.

APPENDIX A: CALCULATION OF PARAMETRIZATION THE FIRST DRIPPING INSTABILITY AGE

A1 Estimation of the unstable sublayer thickness, δ

Considering that the thermal structure in the TBL before destabilization follows the erf function [$T = \mathrm{erf}(z/2\sqrt{t})$], and that the heat flow inside the sublayer remains constant and equal to the heat flow q_{rl} at $z = d_{\mathrm{rl}}$ (see Fig. 6), we can calculate δ, the thickness of the isoviscous sublayer by

$$q_{\mathrm{rl}} = \frac{\Delta T_{\mathrm{ul}}}{\delta}. \tag{A1}$$

For an erf function temperature profile, the heat flow at depth d_{rl} is expressed as follows (see notations in Table 2):

$$q_{\mathrm{rl}} = \frac{\exp\left(-d_{\mathrm{rl}}/2\sqrt{t}\right)^2}{\sqrt{\pi t}}. \tag{A2}$$

Combining eq. (A1) with eq. (A2) yields

$$\delta = \sqrt{\pi t}\,\Delta T_{\mathrm{ul}} \exp\left(\frac{d_{\mathrm{rl}}}{2\sqrt{t}}\right)^2. \tag{A3}$$

Huang *et al.* (2003) suggest that $\exp(d_{\mathrm{rl}}/2\sqrt{\tau_0})^2$ depends on b . In the following, we derive this theoretically, using

$$\Delta T_{\mathrm{ul}} = 1 - \mathrm{erf}\left(\frac{d_{\mathrm{rl}}}{2\sqrt{t}}\right) = \mathrm{erfc}\left(\frac{d_{\mathrm{rl}}}{2\sqrt{t}}\right).$$

Introducing this expression of ΔT_{ul} into eq. (A3), we get

$$\delta = \sqrt{\pi t} \exp\left(\frac{d_{\mathrm{rl}}}{2\sqrt{t}}\right)^2 \mathrm{erfc}\left(\frac{d_{\mathrm{rl}}}{2\sqrt{t}}\right).$$

Furthermore, when the convection is fully developed, the effective temperature drop that drives thermal instabilities beneath the lid is proportional to the viscous temperature scale, with a proportionality coefficient of 2.23 (Morris & Canright 1984; Davaille & Jaupart 1993; Grasset & Parmentier 1998). It therefore yields: $\Delta T_{\mathrm{ul}} = 2.23(-\partial \ln \nu/\partial T)^{-1} = 2.23b^{-1}$ when the sublayer is fully destabilized. Assuming that ΔT_{ul} does not vary with time:

$$\mathrm{erfc}\left(\frac{d_{\mathrm{rl}}}{2\sqrt{\tau_0}}\right) = 2.23b^{-1}.$$

b is equivalent to the Frank-Kamenetskii parameter $Ea^*(T_i^* - T_0^*)/(RT_i^{*2})$, T_0^* being the dimensionalized surface temperature. Therefore, for a realistic situation for the Earth, b should be bracketed between 10 and 19 (depending on the chosen activation energy and internal temperature). This yields, using the previous equation, $0.8 < d_{\mathrm{rl}}/2\sqrt{\tau_0} < 1.1$. As Fig. A1 shows, for $0.8 \leq u \leq 1.1$, $\exp(u^2)\,\mathrm{erfc}(u)$ varies with $0.83[2.23/\mathrm{erfc}(u)]^{-1/4}$, therefore, $\exp(d_{\mathrm{rl}}/2\sqrt{\tau_0})^2\mathrm{erfc}(d_{\mathrm{rl}}/2\sqrt{\tau_0})$ varies with $0.83b^{-1/4}$. Consequently, we approximate the thickness of the unstable sublayer by

$$\delta \simeq A\sqrt{\pi}b^{-1/4}\sqrt{\tau_0},$$

A being equal to 0.83 (see Fig. A1).

A2 Marginal stability

When the unstable sublayer is in a marginal stability state, its local Rayleigh number, Ra_{ul}, is equal to an isoviscous critical Rayleigh

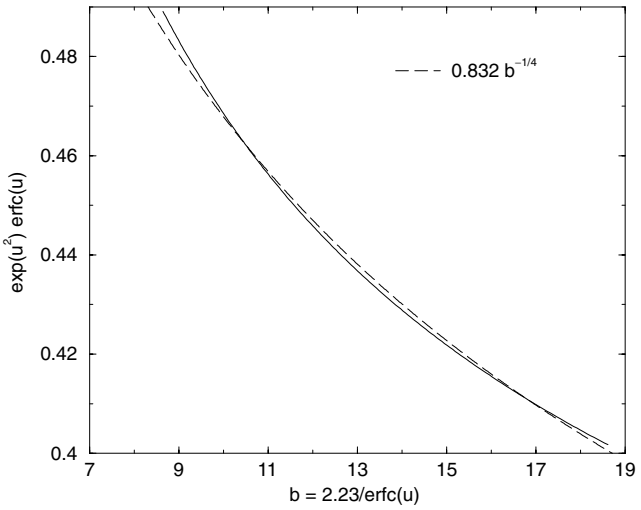

Figure A1. Variations of $\exp(d_{\mathrm{rl}}^2/4\tau_0)\mathrm{erfc}(d_{\mathrm{rl}}/2\sqrt{\tau_0}) = \delta/\sqrt{\pi\tau_0}$ as a function of b , $\exp(b)$ being the viscosity contrast across the fluid layer (black line). The dashed line represents the adjusted curve $\delta/\sqrt{\pi\tau_0} = 0.832b^{-1/4}$.

number, $Ra_{\mathrm{cr-is}}$:

$$Ra_{\mathrm{ul}} = \frac{\alpha\rho g \Delta T^*_{\mathrm{ul}} \delta^{*3}}{K \nu^*_i} = Ra_{\mathrm{cr-is}}.$$

We can then write (see Table 2)

$$Ra_{\mathrm{cr-is}} = \frac{\alpha\rho g T^*_i D^{*3}}{K \nu^*_i} \Delta T_{\mathrm{ul}} \delta^3 = Ra_i \Delta T_{\mathrm{ul}} \delta^3, \tag{A4}$$

where Ra_i is the layer Rayleigh number. Replacing eq. (2) into eq. (A4) and using $\Delta T_{\mathrm{ul}} = 2.23 b^{-1}$, we get

$$\tau_0 \simeq 0.85 \frac{Ra^{2/3}_{\mathrm{cr-is}}}{\pi} Ra_i^{-2/3} b^{7/6}.$$

A3 Perturbations growth rates

For $t > \tau_1$, the growth rate of a perturbation, β, is calculated by the linearization of the convection equations (see Turcott & Schubert 1982 p. 277). As β is very small before the age of first dripping instability, the linearization may be used. It yields

$$\beta(t)\delta(t)^2 \propto Ra_{\mathrm{ul}} - Ra_{\mathrm{cr-is}}. \tag{A5}$$

When time tends towards τ_0, we assume that $Ra_{\mathrm{ul}} \gg Ra_{\mathrm{cr-is}}$. Eq. (A5) then becomes

$$\beta(t)\delta(t)^2 \propto \frac{\alpha\rho g \Delta T^*_{\mathrm{ul}} \delta^{*3}}{K \nu^*_i}. \tag{A6}$$

Using the expression of δ given by eq. (2) in Section 3.1.1 together with eq. (A6) and the expression of the effective temperature drop $\Delta T_{\mathrm{ul}} \propto b^{-1}$, we obtain

$$\beta(t) \propto Ra_i b^{-5/4} \sqrt{t}. \tag{A7}$$

The use of eq. (2) implies that, for $t \leq \tau_0$, the positive growth rates of perturbations are too small to make the temperature profile differ from the erf function.

If E is a quantity defining for example the instability kinetic energy, E varies as $d \ln E/dt \propto \beta(t)$. The first dripping thermal instability is detected when $\ln (E/E_0)$, E_0 being the value of E at $t = 0$, reaches a threshold value called $A_{\mathrm{threshold}}$. Integrating eq. (A7) between $t = 0$ and $t = \tau_0$ yields

$$Ra_i b^{-5/4} \tau_0^{3/2} \propto A_{\mathrm{threshold}}. \tag{A8}$$

Therefore, when the age of the first dripping instability is controlled by the thermal perturbation growth rate, it is parametrized as follows:

$$\tau_0 \propto Ra_i^{-2/3} b^{5/6}.$$

APPENDIX B: MARGINAL STABILITY ANALYSIS OF A SHEARED THERMAL BOUNDARY LAYER

To compute the critical Rayleigh number that applies to the TBL, we solve here for a Newtonian fluid the equations of conservation of mass, momentum and energy. The layer Rayleigh number is defined as

$$Ra_l = \frac{\alpha\rho g \Delta T^* z^{*3}_{\mathrm{BL}}}{\kappa \nu^*_{\mathrm{BL}}},$$

where z^*_{BL} is the layer thickness, ΔT^* the temperature drop across it and ν^*_{BL} the viscosity at its base. Equations below are given in a dimensionless form. Distances, temperature, time, stresses and velocities are scaled by z^*_{BL}, ΔT^*, $z^{*2}_{\mathrm{BL}}/\kappa$, $\nu^*_{\mathrm{BL}}\ \kappa/z^{*2}_{\mathrm{BL}}$ and κ/z^*_{BL}, respectively. The viscosity ν^* is divided by the bottom viscosity ν^*_{BL}. Linearization is obtained by considering that the dimensionless temperature field is the sum of a background state characterized by a given temperature profile $T(z, t)$ and infinitesimal perturbations of this state denoted $\theta(x, z, t)$. These perturbations are associated with stress and velocity perturbations, denoted $\boldsymbol{\sigma}$, $\boldsymbol{v}(x, z) = (v_x, v_z)$, respectively. They correspond to the onset of instability in the TBL. The viscosity depends exponentially on temperature:

$$\begin{aligned}\nu(x, z) &= \exp[b_L(1 - T - \theta)] \approx (1 - b_L\theta)\exp[b_L(1 - T)] \\ &\approx \overline{\nu}(z, t) - b_L\theta\overline{\nu}(z, t),\end{aligned}$$

where $\overline{\nu}(z, t) = \exp[b_L(1 - T)]$ is the unperturbed viscosity profile through the layer. The perturbation in viscosity resulting from the flow onset is $-b_L\theta\overline{\nu}(z, t)$.

The conservation of mass for an incompressible fluid writes

$$\boldsymbol{\nabla}\cdot\boldsymbol{v} = 0. \tag{B1}$$

The conservation of momentum at an infinite Prandtl number leads to

$$\boldsymbol{\nabla}\cdot\boldsymbol{\sigma} + Ra\theta\hat{\boldsymbol{z}} = 0. \tag{B2}$$

The linearized relations between stress and strain rate for a Newtonian rheology yields

$$\sigma_{zz} - \sigma_{xx} \approx 2\overline{\nu}(z, t)\left(\frac{\partial v_z}{\partial z} - \frac{\partial v_x}{\partial x}\right) \tag{B3}$$

and

$$\tau_{\mathrm{xz}} \approx \overline{\nu}(z, t)\left(\frac{\partial v_x}{\partial z} + \frac{\partial v_z}{\partial x}\right). \tag{B4}$$

The linearized conservation of energy writes, for the background state

$$-\frac{\partial T}{\partial t} + \frac{\partial^2 T}{\partial z^2} + H = 0 \tag{B5}$$

and for the perturbations

$$-v_z\cdot\frac{\mathrm{d}T}{\mathrm{d}z} + \nabla^2\theta - \frac{\partial\theta}{\partial t} = 0. \tag{B6}$$

We make the approximation that the thermal structure of the boundary layer is frozen, i.e. we drop the time dependency of $\overline{\nu}$ and T in eqs (B3), (B4) and (B6). Because of this approximation, used in any Ra_{cr} calculation, stability analysis can only be applied to well-developed, slowly cooling, TBLs. The boundary conditions are on the upper and lower boundaries $v_z = 0$ and $\theta = 0$. The upper surface is a fixed boundary with $v_x = 0$ and the lower surface is either free or rigid.

The critical Rayleigh number Ra_{cr} and its associated wavenumber k_c are computed using eqs (B1)–(B4) and (B6) following the method of Buffett *et al.* (1994) and with a top rigid boundary condition and either a free or half-space bottom condition (on top of an infinite half-space of uniform viscosity and without density anomaly, $\tau_{\mathrm{xz}} = 2kv_x$ and $\sigma_{zz} = 2kv_z$, where k is the perturbation wavenumber).

We verify that the code accurately reproduces the known critical Rayleigh numbers for an isoviscous fluid with rigid–free or rigid–rigid boundary conditions. For a layer with a rigid upper surface overlying a viscous half-space, we obtain $k_c = 1.805$ and $Ra_c = 504.8$. The computed values for Ra_c and k_c with rigid–free boundary conditions, a linear temperature profile and a viscosity depending exponentially on temperature correspond to those given by Stengel *et al.* (1982). As in Stengel *et al.* (1982), Ra_c is found to converge towards $20.88 b_L^4$ and k_c towards $0.38 b_L$. For a layer overlying a viscous half-space, Ra_c converges towards $11.74 b_L^4$ and k_c towards $0.32 b_L$.